博士論文（要約）

Dynamics of Atg proteins during autophagosome formation

based on morphological phenotype analysis

（形態表現型解析に基づいたオートファゴソーム

形成における **Atg** タンパク質のダイナミクス**)**

河岡　辰弥

Table of contents

Acknowledgements

I wish to express my heartfelt gratitude to Associate Professor Kuninori Suzuki for his warm support and guidance throughout the research. His intelligible advice and perpetual enthusiasm in research motivated me in my studies.

I would like to convey my sincere gratitude to Professor Yoshikazu Ohya for his support and guidance that made me rethink about this study from a different perspective.

I would like to thank Dr. Eri Hirata, Dr. Shinsuke Ohnuki, Dr. Farzan Ghanegolmohammadi, Dr. Godai Suzuki, Dr. Natsumaro Kutsuna, Dr. Kei Kojo and Mr. Sonei Ri for helping me with experimental and analytical procedure.

I would also like to thank Dr. Hayashi Yamamoto and Dr. Yoshinori Ohsumi for materials.

It gives me great pleasure to acknowledge to the guidance, valuable suggestions and scientific and survival training of Dr. Masatoshi Funabashi.

My deepest gratitude goes to my family for their understanding and support throughout my life. This thesis is impossible without their support. I would like to express my gratitude to my wife, Kana Kawaoka, father, Akiyoshi Kawaoka, mother, Emi Kawaoka, brother, Shingo Kawaoka, grandfathers, Kazuyoshi Kawaoka and Keiichi Takimoto and grandmothers, Yoshie Kawaoka and Akiko Takimoto for their sincere support.

List of Figures

List of Tables

Abbreviations

ALP	· ·	Alkaline phosphatase
AP	· ·	Autophagosome
Ape1	· ·	Aminopeptidase I
ARS	· ·	Autophagy-related structure
Atg	· ·	Autophagy-related
BIC	· ·	Bayesian Information Criterion
ER	· ·	Endoplasmic reticulum
ERES	· ·	Endoplasmic reticulum exit site
GMM	· ·	Gaussian mixture model
IM	· ·	Isolation membrane
MIM	· ·	MIT-interacting motif
MIT	· ·	microtubule-interacting and transport
PC	· ·	Principal component
PCA	· ·	Principal component analysis
PI3-kinase	· ·	Phosphatidylinositol 3-kinase
PI3P	· ·	Phosphatidylinositol 3-phosphate
prApe1	· ·	premature form of aminopeptidase 1
Qautas	· ·	Quantitative autophagy-related structure analysis system
TORC1	· ·	Target of rapamycin complex I
VICS	· ·	Vacuole IM contact site

Abstract

Autophagy is a degradation system that recycles intracellular components conserved in eukaryotic cells. In the yeast *Saccharomyces cerevisiae*, **au**to**t**opha**g**y-related (Atg) proteins essential for **a**uto**p**hagosome (AP) formation form a restricted punctate structure near the vacuole to expand **i**solation **m**embranes (IMs), which mature to become enclosed APs. Recently, our group has shown that these Atg proteins play a critical role in IM expansion by developing an IM visualization technique under a fluorescence microscope. Thus, morphological analysis of **a**utophagy-**r**elated **s**tructures (ARSs) including IMs is a powerful method for understanding the mechanisms of AP formation. However, this method was performed manually and was time-consuming. The only fully expanded IMs were subjected to the analysis. Therefore, the high-throughput and comprehensive analyses of ARSs were awaited. To analyze the process of AP formation comprehensively, I developed a high-throughput morphological analysis system for ARSs with a combination of image analysis and machine learning, which named **Q**uantitative **au**tophagy-related structure **a**nalysis **s**ystem (Qautas). Qautas can analyze morphological features of IMs much faster than a conventional manual method with equal detection accuracy.

Atg1 is a multi-functional protein that has a scaffolding function and a kinase activity. *atg1*^{D211A} cells are defective in the kinase activity but has the scaffolding function, whereas *atg1*Δ cells have neither function. In *atg2*Δ cells, both functions of Atg1 are

normal although AP formation is absolutely inhibited. Qautas can classify ARS in IM visualized cells as elongated ones or dot-shaped ones. Morphometric analysis of ARSs in wild-type cells and autophagy mutants (*atg1Δ, atg1*[D211A] and *atg2Δ* cells) by Qautas showed that the frequency of elongated structures markedly increased in wild-type and *atg1*[D211A] cells but not in *atg1Δ* and *atg2Δ* cells. Next I analyzed the elongated structures by **p**rincipal **c**omponent **a**nalysis (PCA) and hierarchical clustering, resulting that the elongated ones were divided into six groups. I found that the clusters including large cup-shaped structures were only present in wild-type cells. The majority of elongated structures belonged to the clusters including small bar-shaped structures. From these analyses, I succeeded to separate morphological phenotypes among wild-type, *atg1Δ*, *atg1*[D211A] and *atg2Δ* cells, which could not be distinguished previously. This analysis suggests that the scaffold function and kinase function of Atg1 act different steps in AP formation. Moreover, I found that Atg2 did not localize to ARSs in *atg1*[D211A] cells. This indicates that Atg1 is involved in localization of Atg2 through its kinase activity.

In W303 diploid cells, APs can be visualized without IM visualization. The major advantage using W303 diploid cells is that the whole process of autophagy, which are IM expansion, AP maturation, fusion to the vacuole, and degradation of autophagic bodies inside the vacuole, can be traceable using Atg8 as a marker of ARSs. ARSs were extracted from autophagy-induced W303 diploid wild-type cells, and their morphological parameters were analyzed with the **G**aussian **m**ixture **m**odel (GMM), resulting that the ARSs were separated into seven morphological clusters. I noticed that two of seven clusters were found only in wild-type cells. Thus, I conclude that these clusters are AP clusters.

Next, I focus on the ARSs in AP clusters. Localization analysis of Atg proteins to the ARSs revealed that Atg1, Atg8, Atg17 and Atg29 had puncta at the contact site between the vacuole and ARS. Atg2 is known to localize at the edge of IMs as multiple puncta during IM expansion. I found that Atg2 still localized to the ARS in the AP clusters as multiple puncta.

Previously, it has been widely believed that APs are formed through the following steps; assembly of Atg proteins, assembly of membranes (nucleation), IM expansion and IM closure. In this model, an AP is always formed via the cup-shaped IM as an intermediate structure. Time-lapse morphological analysis of ARSs revealed that after spherical ARS emerged, they gradually increased in volume with keeping their high roundness, and finally fused to the vacuole. Astonishingly, this observation suggests that the large IM does not appear during AP formation. Rather, this suggests that APs are inflated after nucleation. In this study, I propose a novel model of AP formation without large IMs, that is, the inflation after nucleation model.

General Introduction

Macroautophagy, (hereafter referred to as autophagy) is a bulk degradation system that highly conserved among eukaryotes. It is important for balancing degradation and biosynthesis to keep homeostasis of cells (Mizushima et al., 2011). Targets of autophagy are not only proteins and organelle but also pathogens that invade into cells (Mizushima and Komatsu, 2011). It has been reported that autophagy is related to several incurable diseases such as Parkinson's diseases, Alzheimer's diseases, Crohn's diseases and cancer (Banerjee et al., 2010; Rioux et al., 2007; White, 2012). Autophagy modulation has a possibility to cure those intractable diseases (Rubinsztein et al., 2012). However the basal mechanism that performs autophagy has poorly understood, hence the mechanical analysis has been needed. Accumulation of Atg proteins to a restricted perivacuolar site is a first step of AP formation in yeast (Kirisako et al., 1999; Suzuki et al., 2001) (Fig. 1). The IM, a cup-shaped membrane structure expands and encloses cargoes to be degraded (Kirisako et al., 1999). Subsequently, the IM matures to become a double-membrane compartment called an AP, the outer membrane of an AP fuses with the vacuole membrane (Baba et al., 1994). The digestive enzymes degrade the inner membrane structure, an autophagic body, derived from an AP and its contents diffuse throughout the vacuole (Nakatogawa et al., 2009). It is known that 19 Atg proteins are critical for AP formation (Araki et al., 2013; Mizushima and Komatsu, 2011; Tsukada and Ohsumi, 1993). Morphological phenotypes of expanding IMs in those Atg proteins mutants are very difficult to separate in electron microscopy, because all mutants showed defect of AP formation. Thus, a method to

discriminate IMs from other autophagic structure by fluorescence microscopy was long awaited.

IMs can be visualized with overexpression of the **pr**emature form of **a**mino**pe**ptidase **1** (prApe1), a selective cargo of autophagy and observation of Atg8, a marker of ARSs (Suzuki et al., 2013). This study describes three patterns in the localization of other Atg proteins, the **v**acuole-**I**M **c**ontact **s**ite (VICS) pattern, IM-Edge pattern and IM pattern in **A**mino**pe**ptidase **I** (Ape1) overexpressing cells (Suzuki et al., 2013). This IM visualization technique enables us to examine morphological phenotypes of IMs during AP formation. The result of measurement of IM lengths in autophagy mutants are in accord with autophagic activity estimated by the **al**kaline **p**hosphatase (ALP) assay, which reflects bulk autophagic activity (Noda et al., 1995; Noda and Klionsky, 2008). Morphological analysis of autophagy mutants and localization analysis of Atg proteins revealed that intra-organellar interaction is important for AP formation and Atg proteins have several localization patterns reflecting their functions. However, dynamics of Atg proteins during AP formation remains unknown.

Atg proteins change their localization during IM expansion and contact with other organelles such as the ER and vacuole. However, localizations of Atg proteins on the APs are still unknown. Visualization of Atg proteins on the AP will lead to a novel model of AP formation.

Part I

Morphological analysis of ARSs at the early stage of AP formation

Introduction

It is known that 19 Atg proteins essential for AP formation can be divided into five functional units (Nakatogawa et al., 2009), the Atg1 kinase complex, phosphatidylinositol 3-kinase (PI3-kinase) complex I, Atg12 conjugation system, Atg8 conjugation system and membrane protein complex (Fig. 2). The localizations of Atg proteins are basically consistent with the functional units (Suzuki et al., 2013) (Fig. 3). The Atg1 complex and PI3-kinase complex localize at the VICS, ubiquitin-like conjugation systems (Atg8-binding proteins and Atg12-binding proteins) localize throughout the IM, and the membrane protein complex localizes at the IM edges. On the other hand, it is reported that only Atg1 transits to the IM among the components of the Atg1 complex (Suzuki et al., 2013), indicating that Atg1 has an additional role during IM expansion.

When cells face with starvation, the target of rapamycin complex I (TORC1) receives a starvation signal and becomes inactivated (Fig. 4). Then, Atg13 is dephosphorylated and binds to Atg1. The Atg1-Atg13 complex binds to the Atg17-Atg29-Atg31 complex and it works as a scaffold of the ARS (Kawamata et al., 2008, Chew et al., 2015). Atg1 is an only protein kinase among Atg proteins. The kinase activity

of Atg1 is elevated by the formation of the scaffolding complex (Kamada et al., 2000). Atg1 has a kinase domain at the N-terminal region (Matsuura et al., 1997), and the kinase activity of Atg1 is activated through its autophosphorylation (Kijanska et al., 2010). The $atg1^{D211A}$ strain, which lacks the kinase activity, is defective in autophagy (Yeh et al., 2010). A recent study has revealed that activated Atg1 phosphorylates Atg9 and is involved in lipid recruitment (Papinski et al., 2014). At the C-terminal region of Atg1, there is a tandem repeat of **m**icrotubule-**i**nteracting and **t**ransport (MIT) domains that consist of three α-helices and bind to the **M**IT-**i**nteracting **m**otif (MIM) domain of Atg13 (Fujioka et al., 2014; Jao CC et al., 2013; Noda and Fujioka, 2015). This interaction is important for formation of scaffolding complex and progression of autophagy. Mutations in the Atg1 MIT domain and the MIT binding domain of Atg13 cause a defect in the formation of the scaffold complex, leading to a defect in Atg1 autophosphorylation. Atg1 is a multi-functional protein that has a scaffolding function and a kinase activity, but the precise functions of both domains are still remaining unrevealed.

The mechanisms of IM expansion have been unknown because of the complicated interactions among 19 Atg proteins. Besides, there has been no way to analyze expanding IMs because ARSs were too small to observe by fluorescence microscopy and the ARSs were not recognized by electron microscopy. A previous study revealed that Atg1 kinase mutants ($atg1^{K54A}$, $atg1^{D211A}$) had short IMs by morphological analysis of ARSs in IM visualized cells (Suzuki, 2013). Development of an IM visualization technique suggests a possibility to be a breakthrough of the morphological analysis of ARSs including IMs, but

there were some problem in quantification steps; quantification was performed manually (Fig. 5). During the manual quantification of ARSs, it took about 10 minutes to analyze one structure. Thus, I aim to develop a high-throughput measurement system of the morphological features of ARSs and to perform the comprehensive morphological analysis of ARSs in wild-type cells and autophagy mutant cells. This analysis will provide new insight into the mechanisms of IM expansion.

Results

Development of high-throughput ARS morphological analysis system

To develop the high-throughput measurement system of the length of ARS, I tried to measure the length using image analysis (Fig. 6). Wild-type, $atg1^{D211A}$ and $atg1^{K54A}$ cells were used to test the detection accuracy of the system. $atg1^{D211A}$ and $atg1^{K54A}$ are kinase mutants of Atg1 and those mutants showed shorter maximum lengths than wild-type (Suzuki et al., 2013). $atg1^{K54A}$ has a weak autophagic activity and shows a slightly longer maximum length than a kinase-dead mutant, $atg1^{D211A}$. With only an image analysis, any difference in the structure lengths of these strains was not detected (Fig. 7 A). Histograms of the length showed that there were a large amount of small-sized structures in each strain (Fig. 7 B). These small-sized structures were recognized as small dot-shaped structures, which seemed unlikely the IMs, under a fluorescence microscope. Thus, I think that the detection accuracy would increase by removing small dot-shaped structures from analysis.

To remove dot-shaped structures, the machine learning algorism, Random Forest was implemented in the procedure (Fig. 8). The discriminator of dot-shaped and elongated structures was created using a half of the training data (study data). The accuracy of this discriminator was estimated as 91.5% using the remaining half of the training data (test data). After discrimination, lengths of the classified structures were compared in each strain. Comparison of the lengths of dot-shaped structures showed that there were no significant differences among the structures in these strains (Fig. 9 A). But the lengths of elongated structures in $atg1$ mutants were shorter than that of wild-type cells. Furthermore, $atg1^{D211A}$

16

cells had shorter elongated structures than $atg1^{K54A}$ cells (Fig. 9 C). This result well correlates with a previous study (Suzuki et al., 2013). This system could measure over 100 structures in 10 minutes. With a conventional manual method, it took 10 minutes per one structure. Thus, this new system is 100 times faster than the conventional method with an accuracy of the similar level. I name this system as the Qautas.

Qautas reveals the dynamics of ARSs

Qautas can rapidly and comprehensively analyze the ARSs in fluorescence microscopic images. The frequency of ARSs increased just after autophagy induction and reached a peak at 1.5 h (Fig.10 A). Subsequently, the frequency slightly decreased and reached a steady state. This might reflect that the biogenesis and degradation of APs come to equilibrium in wild type cells. Frequencies of dot-shaped and elongated structures reached a peak at 1 h and 1.5 h, respectively (Fig.10 B, C). This suggests that at least a part of dot-shaped structures are transformed into elongated structures in 30 minutes.

The frequency of elongated structures markedly increased in $atg1^{D211A}$

To analyze morphological difference between autophagy defective mutants, ARSs of *atg1* and *atg2* mutant were analyzed. It is considered that the kinase activity of Atg1 works after the scaffolding function of Atg1 (Kawamata et al., 2008). Atg2 localizes on the edge of IM and tethers ER and IM (Suzuki et al., 2013, Kotani et al., 2018). It is considered that Atg2 is essential for the IM expansion because lipids stained by R18 are not transferred into IM in *atg2*Δ cells (Hirata et al., 2017). However, morphological

17

differences among in *atg1Δ*, *atg1*[D211A] and *atg2Δ* cells were still known. Qautas has possibility to separate the morphological difference of ARSs between *atg1* deleted (*atg1Δ*) cells and *atg1* kinase-dead (*atg1*[D211A]) cells. The frequencies of ARSs in *atg1Δ*, *atg1*[D211A] and *atg2Δ* cells were analyzed. The *atg2Δ* cells are analyzed as another autophagy defect strain.

The frequencies of dot-shaped structures were increased after autophagy induction in each strain (Fig. 11 B, E, H). The frequency of elongated structures was slowly increased in *atg1Δ* cells (Fig. 11 C) and was markedly increased in *atg1*[D211A] (Fig. 11 F). But in *atg2Δ*, the frequency of elongated structures did not increased (Fig. 11 I). Using Qautas, frequencies of ARSs could be analyzed and phenotype of *atg1*[D211A], *atg1 Δ* and *atg2Δ* were different.

Elongated structures in *atg1 Δ* and *atg1*[D211A] cells are bar-shaped structures

It has been thought that *atg1Δ* and *atg1*[D211A] strain could not expand IMs. But elongated structures were increased in *atg1Δ* and *atg1*[D211A] cells. So, I analyzed morphological differences between ARSs formed in these mutants. In microscopic images, large cup-shaped structures were observed in wild-type cells but not in *atg1Δ* and *atg1*[D211A] cells (Fig. 12). Instead of large cup-shaped structures, small bar-shaped structures were observed in *atg1Δ* and *atg1*[D211A] cells. To analyze morphological differences of elongated structures observed in wild-type, *atg1Δ* and *atg1*[D211A] cells, quantified morphological parameters were compared. There were significant differences between wild-type and autophagy mutants in parameters that were related to the circularity of structures (axis ratio

and roundness) (Fig.13 A, B). Parameters that related to the size of structures (Area, Perimeter and Major axis length) were significantly larger in wild-type cells compared with autophagy mutants (Fig.13 C, D, E). Remarkably, there were significant differences in Area", "Perimeter" and "Major axis length" parameters of structures in *atg1Δ* and *atg1*^{D211A} cells, suggesting that elongated structures in *atg1Δ* and *atg1*^{D211A} cells are morphologically different. Taken together, I conclude that elongated structures observed in wild-type, *atg1Δ* and *atg1*^{D211A} cells have different morphological features.

Elongated structures in wild-type cells are classified into six morphological clusters

To examine the differences among the elongated structures observed in wild-type *atg1Δ*, *atg1*^{D211A} and *atg2Δ* cells, nine morphological parameters of elongated structures were subjected to the PCA. The loadings of each **p**rincipal **c**omponent (PC) were listed in Table 3. PC1 to PC4 contributed to compress the over 90% of variance in quantified data (Fig. 14 A). Next, all the elongated structures were clustered using PC1 to PC4 (Fig. 14 B). The elongated structures were divided into six clusters with hierarchical clustering using Euclidean distances. The cluster 1 is a group of elongated structures that are small bar-shaped (Fig. 14 C). The structures in the cluster 2 showed a thick and highly bent cup-shaped form. The structures in the cluster 3 were thin bar-shaped. The structures in the cluster 4 were long and thick bar-shaped. The structures in the clusters 5 and 6 were large cup-shaped and the curvature and minor axis length of the ones in the cluster 5 were larger than those of cluster 6 (Fig. 14C, Table 3).

The frequency of six morphological clusters

As shown above, the elongated structures have divided into six clusters based on their morphological parameters (Fig. 14). Next, the elongated structures in wild-type, *atg1Δ*, *atg1*[D211A] and *atg2Δ* cells were clustered and analyzed. The vast majority of elongated structures were small bar-shaped structures belonging to the cluster 1 (Fig. 15 A). The clusters 5 and 6 appeared only in wild-type cells indicating that large cup-shaped structures are formed in wild-type cells but not in autophagy mutants (Fig. 15 B). In addition to the clusters 5 and 6, the cluster 4 did not appear in *atg2Δ* cells. In Figure 11 F, the frequency of elongated structures markedly increased in *atg1*[D211A] cells. The ratios of the cluster 1 structures were particularly high in *atg1*[D211A] cells (Fig. 15 A). The frequencies of the cluster 1 structures in *atg1*[D211A] cells increased similarly as wild-type cells until 1.5 hours after autophagy induction. However, the frequency increased until 3 hours and reached a plateau (Fig. 15 C). Time-lapse image acquisition of wild-type revealed that a dot-shaped structure appears at the beginning and becomes a bar-shaped structure belongs to the cluster 1. Then it finally becomes a cup-shaped IM (Fig. 16). These results indicate that the cup-shaped IM formation is normal only in wild-type cells (Fig. 17). Bar-shaped structures are formed and accumulated in an Atg1 scaffold function dependent manner.

The kinase activity of Atg1 kinase is essential for Atg2 localization and lipid transfer

Atg2 is a lipid transfer protein (Osawa et al., 2018) and lipids stained with R18 are not transferred to IMs in *atg2Δ* cells (Hirata et al., 2017). It is known that Atg1 is essential for Atg2 localization to the ARS (Suzuki et al., 2007). To understand if the kinase activity of Atg1 affects lipid recruitment into ARSs, colocalization of R18 with ARSs were examined (Fig. 18). Lipid transfer from ERES to IM was impaired in *atg1*[D211A] and *atg1Δ* cells. R18 stained lipids could not localize on the ARS without Atg1 kinase activity. It is already known that Atg2 loses its localization to the ARS in *atg1Δ* cells (Suzuki and Ohsumi, 2007). To test if Atg2 localization is depending on Atg1 kinase function, Atg2 localization in *atg1*[D211A] cells were observed (Fig. 19). Atg2 lost its localization to the ARS in *atg1*[D211A] cells. That result indicates that Atg1 kinase function is essential for Atg2 localization and transport of R18 positive lipids. So, localization of Atg2 is essential for the R18 staining of ARSs.

Discussion

Qautas analyzes ARSs in quickly and objectively

Visualization and morphological analysis of ARS had been powerful tool for phenotypic analysis for autophagy mutants (Suzuki et al., 2013). However, only fully expanded IMs are subjected to the analysis because morphological features are measured by manually. To perform the high-throughput and objective morphological analysis for ARS, I developed a system to measure the length of ARSs by using only image processing (Fig. 7). However, it was impossible to detect the difference of the length among wild-type and *atg1* mutants. Focusing on the histograms of the length, it is assumed that there are so many structures that have short length in each strain. Seeing microscopic images realizes me that there were so many dot-shaped structures in each strains. This result implies that many ARSs stay as dot-shaped structure before IM expansion and Atg proteins assembly takes time to assemble essential materials for IM expansion. So, measuring all structures containing dot-shaped structures is inadequate for this analysis. I need to focus on the morphological phenotype of elongated ARSs. Next, I developed the discrimination system of dot-shaped structure and elongated structure using machine learning algorism, random forest (Breiman, 2001) (Fig. 8). With this system I can automatically discriminate ARSs before or after expansion. After discrimination, this system detected difference between wild-type, *atg1*[D211A] and *atg1*[K54A] with over 100 times efficiency. And this system analyzes the all structures captured in microscopic images that had been impossible with conventional method (Kawaoka et al., 2017). The strengths of this system are the speed and

objectivity of the quantification. Combination of IM visualization and Qautas has

possibility to perform the comprehensive analysis of morphological features of ARSs.

Those detailed and comprehensive analysis might obtain the new findings about

complicated mechanisms of IM expansion. In this system, all ARSs were discriminated into

two structures based on training data made by human. This is a disadvantage of Qautas and

clustering with data-driven method could be the solution for this problem.

Small bar-shaped structures are formed in an Atg1 scaffold function dependent

manner

In previous method, most of elongated ARS had been ignored because measuring

all structures is time consuming. After development of Qautas, it has become possible to

analyze objective phenotypic analysis of all elongated ARSs. The time-dependent change in

frequency of ARS reflected the dynamics of AP formation in wild-type cells (Fig. 10). The

remarkable increase of elongated structures was observed in wild-type and $atg1^{D211A}$ cells

after 1.5 hours of autophagy induction (Fig. 10 C, Fig. 11 F). But it wasn't observed in

$atg1\Delta$ (Fig. 11 C). The scaffold function of Atg1 may contribute the formation of elongated

structures just after the autophagy induction.

The results of microscopic observation (Fig. 12) and comparison of quantified

morphological parameters (Fig. 13) showed that the elongated structures contain typical IM

structure, cup-shaped structures and newly characterized structure, bar-shaped structures.

To analyze those structures separately, elongated structures were subjected to PCA and

hierarchical clustering and divided into 6 morphological clusters (Fig. 14). The groups of

large cup-shaped structures, cluster 5 and cluster 6 observed only in wild-type cells (Fig. 15 B). Comparison of the frequency of cluster 1 in wild-type and $atg1^{D211A}$ cells showed that the small bar-shaped structures, cluster 1 accumulated in $atg1^{D211A}$ cells (Fig. 15C). After autophagy induction, $atg1^{D211A}$ cells showed constant increase until 3 hours and reached a plateau while wild-type cells settled the steady state. This may reflect the dynamics of AP formation had stacked at some point in $atg1^{D211A}$ cells. The small bar-shaped structures accumulated in an Atg1 kinase dependent manner. It reflects that the Atg1 scaffold function acts at very beginning of AP formation and form the scaffold complex before IM expansion. Qautas succeed to detect subtle difference between ARS with or without the Atg1 scaffold function.

Atg1 kinase activity is essential for Atg2 localization and R18 localization to the ARS

R18 staining analysis in $atg1^{D211A}$ and $atg1\Delta$ cells revealed that the Atg1 kinase function is essential for the lipid transfer from ERES to ARS (Fig. 18). The Atg1 kinase function is essential for the Atg2 localization to the ARS (Fig. 19). Atg2 works as the tethering factor of ER and IM (Kotani et al., 2018). Atg2 transfers lipids *in vitro* (Osawa et al., 2018). Atg2 is responsible for the transfer of R18 stained lipid to the ARS (Hirata et al., 2017). So, the Atg1 scaffold function is essential at the initial step of AP formation and the Atg1 kinase function is essential at the IM expansion step via localization of Atg2 (Fig. 20). It is reported that the Atg1 kinase phosphorylates Atg2 and Atg9 in vitro (Papinski et al., 2014). $atg1^{D211A}$ cells showed accumulation of Atg9 to the ARS (Reggiori et al., 2004). Considering these reports, the kinase function of Atg1 is essential for the IM expansion step

24

because it regulates Atg2, Atg9 and Atg18 localization and dynamics (Suzuki et al., 2007; Suzuki et al., 2013). The Atg1 kinase function is essential for the Atg2 localization to the ARS. Formation of Atg2, Atg9 and Atg18 complex at edges of IMs are essential for an intra-organellar interaction between ER and ARS. The objective morphological analyses of ARS succeed to detect subtle differences among *atg1* mutants. It has also uncovered that functions of Atg1 as the member of scaffold complex and the protein kinase may act in different steps of the AP formation.
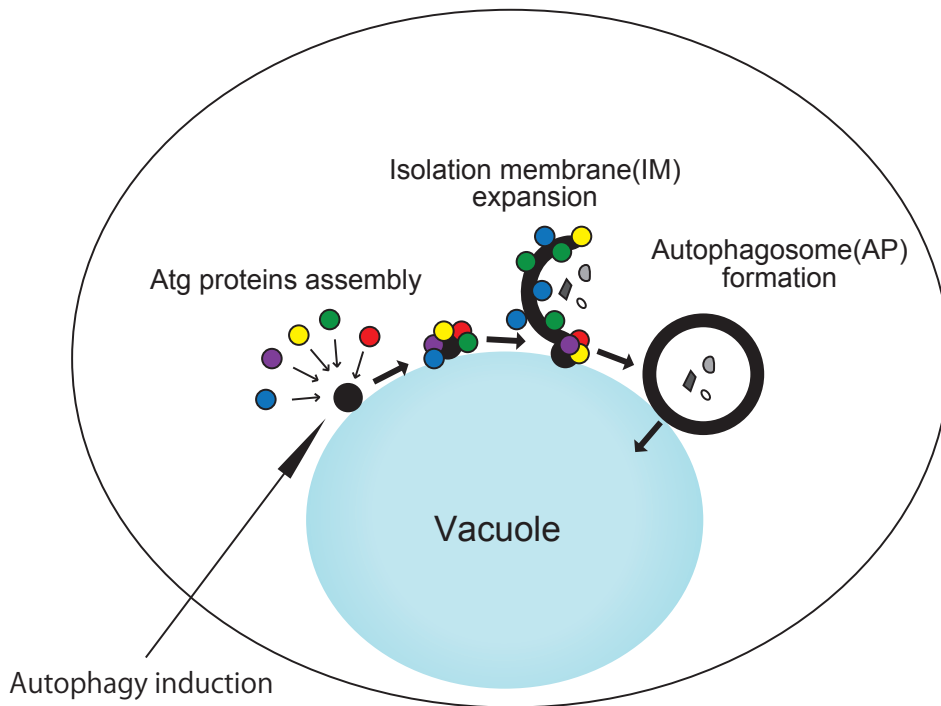
Figures

Fig. 1. Model for the process of autophagy

After induction of autophagy with starvation or rapamycin treatment, Atg proteins are assembled at the restricted position on the surface of vacuole. Subsequently, IM expands to enclose degradation targets and forms AP.
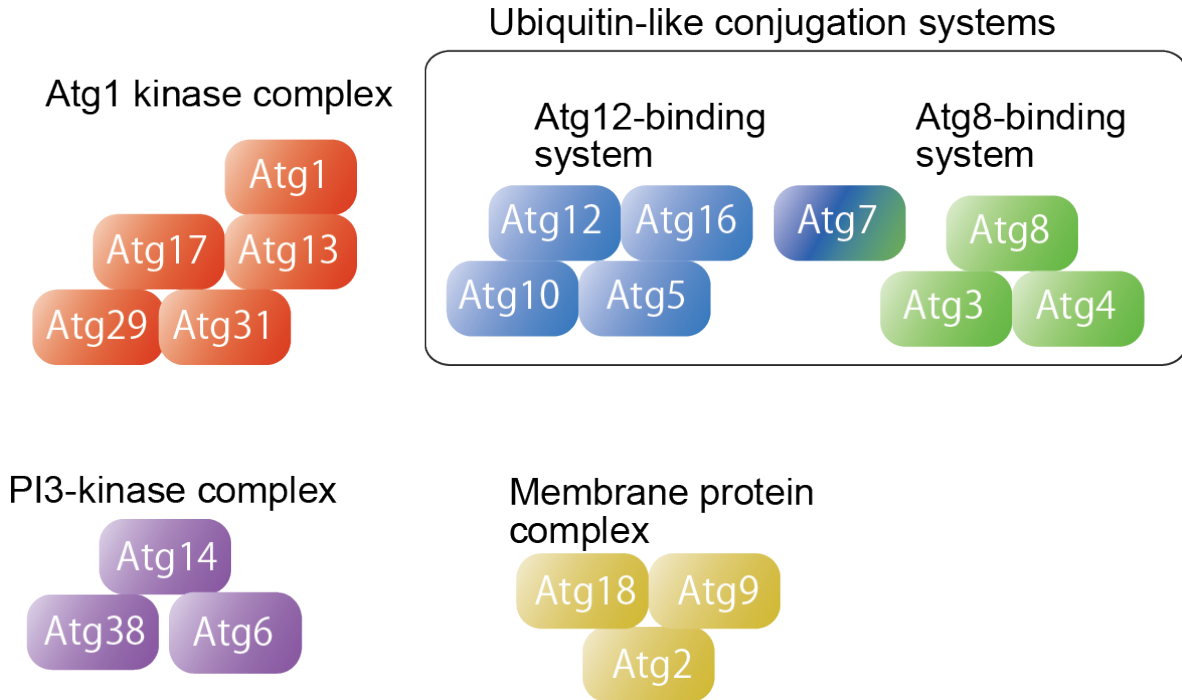
Fig. 2. Functional units of Atg proteins

Essential 19 Atg proteins can be separated into 5 functional units. The Atg1 kinase complex plays a role as a scaffold of Atg proteins assembly. The PI3 kinase complex interacts with Vps15 and Vps34. There are two ubiquitin-like conjugation systems, Atg12-binding proteins and Atg8-binding proteins. Atg9 is a sole transmembrane protein among Atg proteins. It is known that Atg2 and Atg18 bind to Atg9 but their molecular functions are poorly understood.
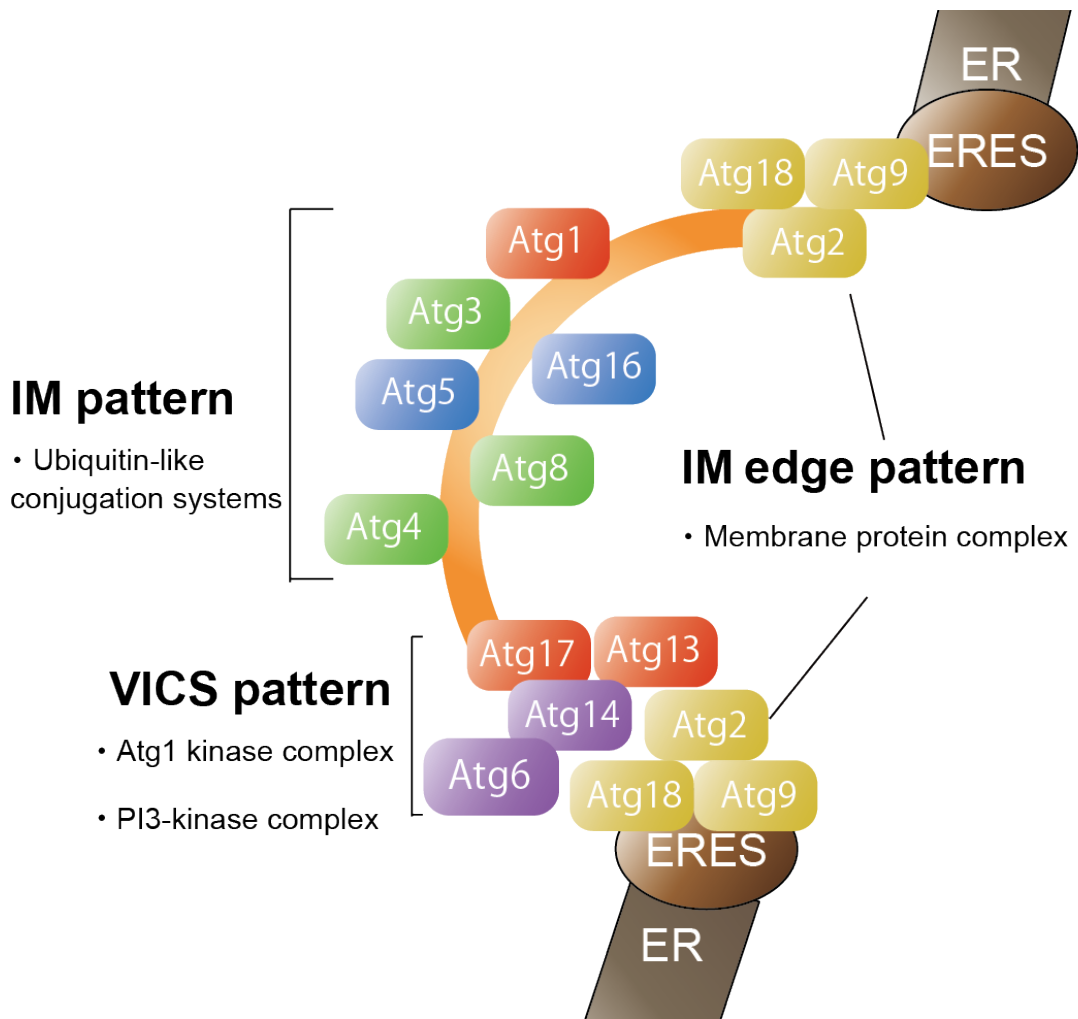
Fig. 3. Localizations of Atg proteins during IM expansion.

Atg proteins show different patterns of localization during IM expansion. The Atg1 kinase complex and PI3 kinase complex localize to the VICS. The membrane protein complex localizes at the edges of the IM near the **e**ndoplasmic **r**eticulum **e**xit **s**ite (ERES). Two ubiquitin-like conjugation systems and Atg1 localize to the entire IM.
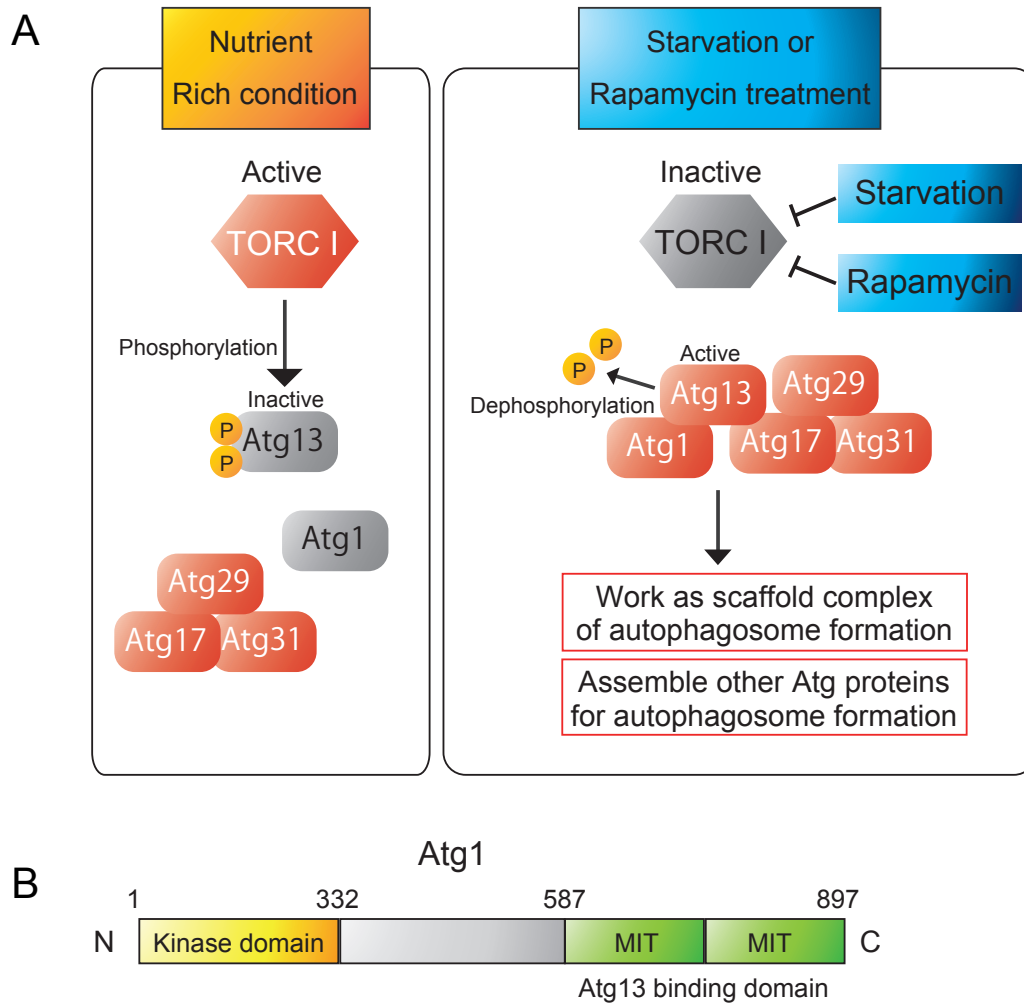
Fig. 4. Regulation and functional domains of Atg1

(A) Regulation of the Atg1 complex after nutrient starvation or rapamycin treatment.

Under nutrient rich conditions, Atg13 is phosphorylated by TORC1 and kept inactivated.

By nutrient starvation or rapamycin treatment, TORC1 becomes inactivated and Atg13 is

dephosphorylated. Dephosphorylated Atg13 binds to Atg1 to form the Atg1 complex

including Atg13, Atg17, Atg29 and Atg31. (B) Functional domains of Atg1. Atg1 has a

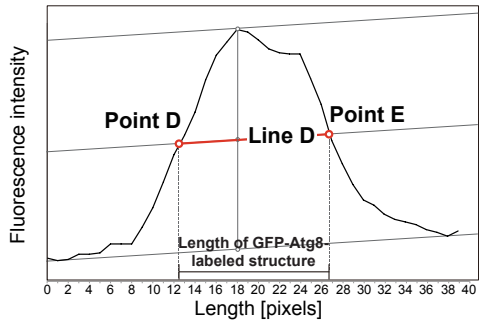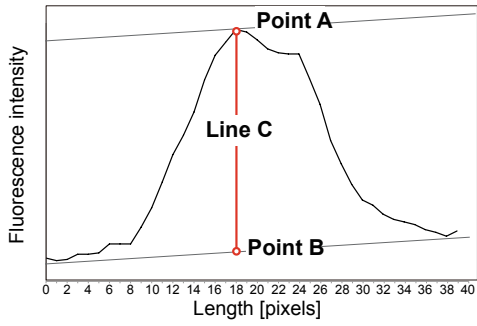kinase domain at the N-terminal region and an Atg13 binding domain at the C-terminal
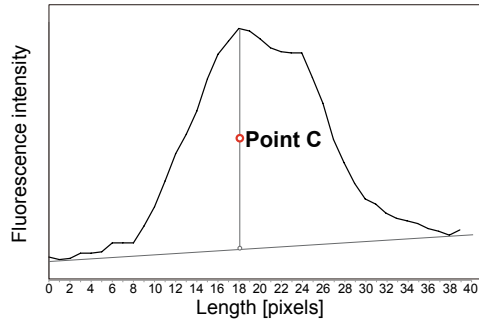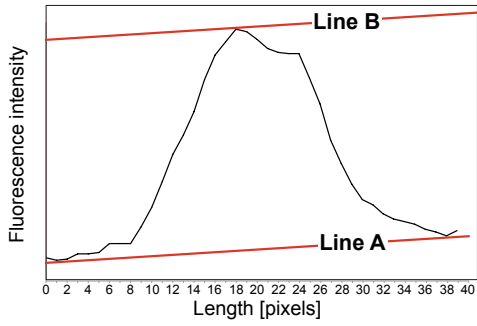
region.
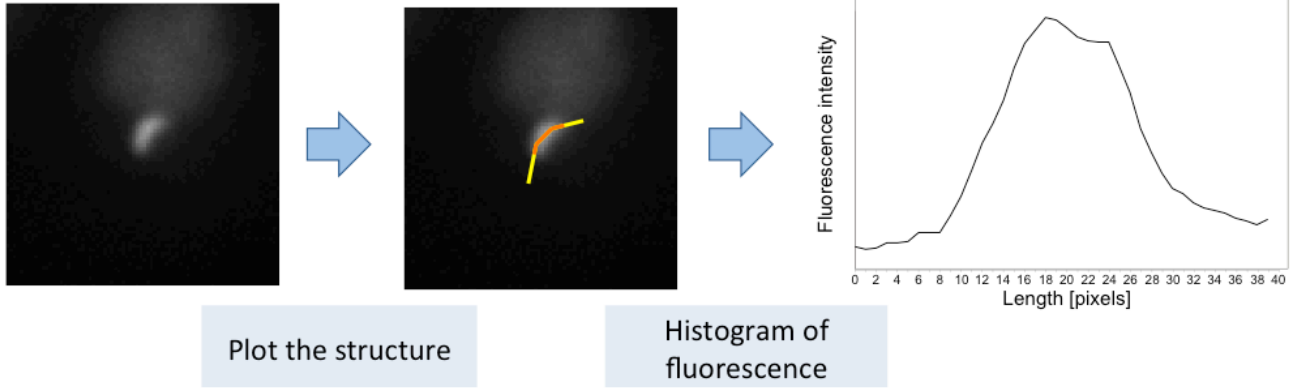
Fig. 5. Manual method to measure the length of ARSs

(A) Histogram of fluorescence intensities was extracted from the cup-shaped structure. (B) The manual method to measure the length of ARSs. Draw a background lines (Line A) and its parallel line (Line B) through the maximum value of the intensity. Add a line vertical to the X-axis (Line C) from the maximum value point (Point A). Point the intersection of Line A and Line C (Point B). Calculate the middle point of Point A and B (Point C). Draw a line parallel to the background line through the Point C (Line D). Point the intersections of the intensity profile and Line D at two points (Point D and E). Measure the distance on the X-axis between Points D and E.
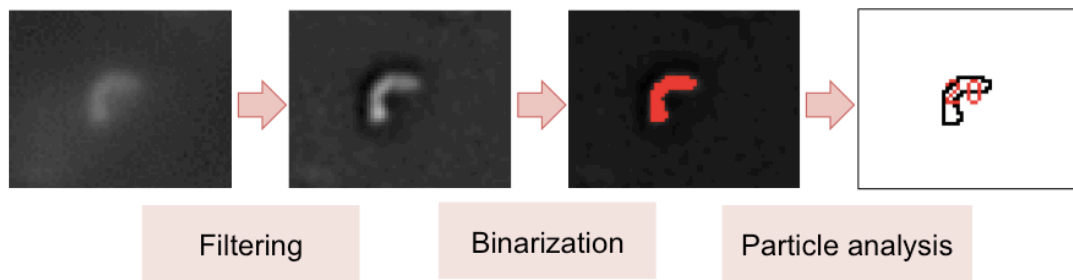
Parameters

Area

Perimeter

Majour Axis

Minor Axis

Angle

Circularity

Axis ratio

Roundness

Solidity
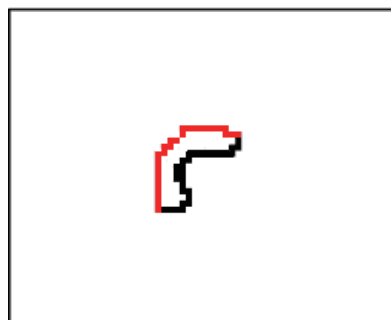
A half value of perimeter

Fig. 6. Automatic method to measure the length of ARSs by image analysis

At first, microscopic images were normalized with its fluorescence intensities, then filtered by a bandpass filter to emphasize ARSs. Finally, ARSs were extracted by binarization. Nine morphological parameters were extracted from the ARSs by particle analysis.
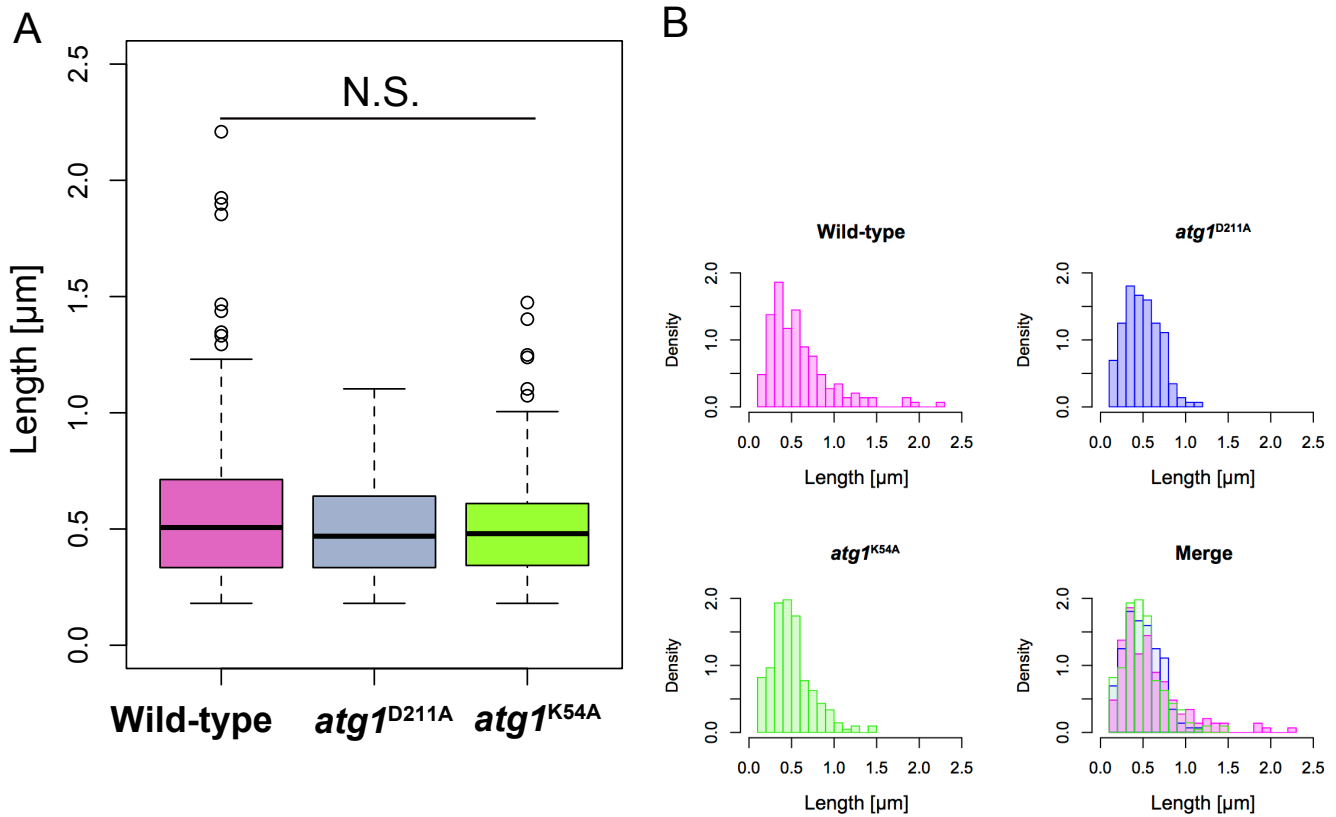
Fig. 7. Comparison of the size of ARSs

After extraction of IM length, perimeters of ARSs were compared as an index of the structure length. ARSs in wild-type, $atg1^{K54A}$ and $atg1^{D211A}$ were analyzed. $atg1^{D211A}$ is a kinase-dead mutant and the $atg1^{K54A}$ is a leaky kinase-defective mutant. (A) Comparison of the structure length. ARSs in $atg1$ mutants showed significantly short structure length. There was no significant difference between ARSs in $atg1^{K54A}$ and $atg1^{D211A}$. (B) Distribution of structure length data. There were some structures which has longer structure length in $atg1^{K54A}$ than in $atg1^{D211A}$. $*P < 0.05$; $**P < 0.001$; N.S. (not significant) indicates $P > 0.05$ (two tailed Student's t-test).
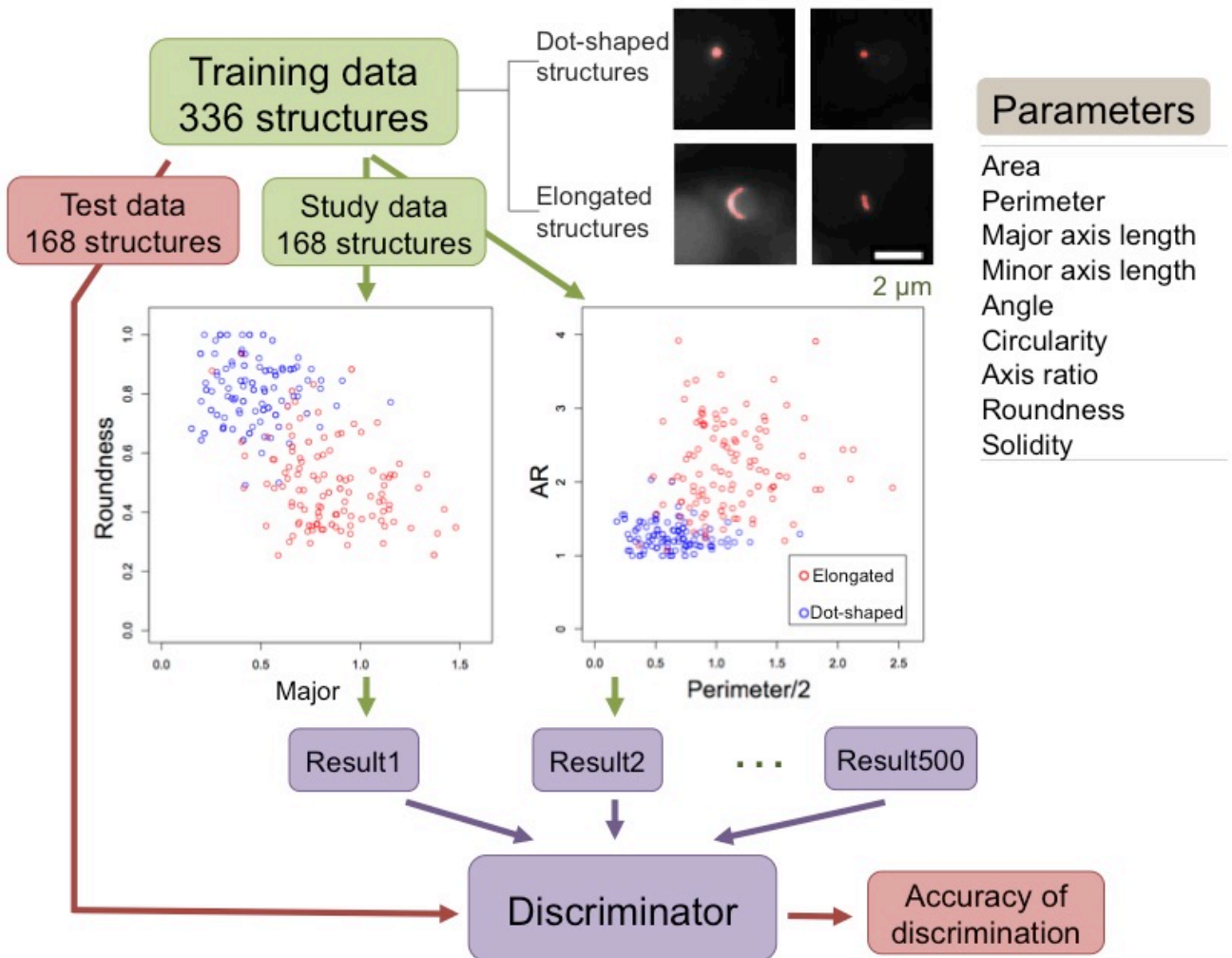
Fig. 8. Scheme of randomForest discrimination

Nine morphological parameters (area, perimeter, majorr length, minor length, angle, circularity, axis ratio, roundness and solidity) of ARSs were extracted by image analysis. 336 structural data were discriminated into elongated structures, which contain IMs, or dot shaped structures, which contain the VICS manually. Half of them were used for learning of discriminator and the other half were used for accuracy verification of discriminator. Discriminator had been made of group learning of 500 weak learners (decision trees), which can discriminate unclassified data into the IM or VICS based on the training data.
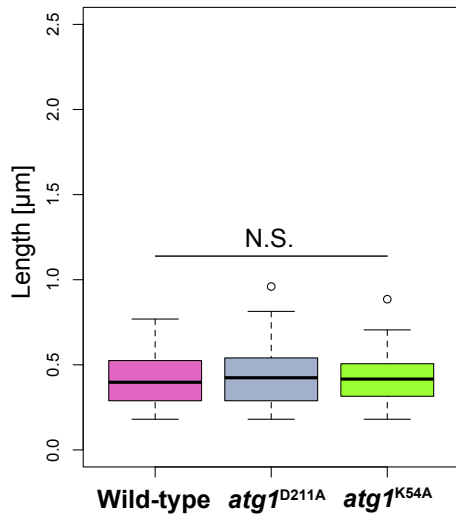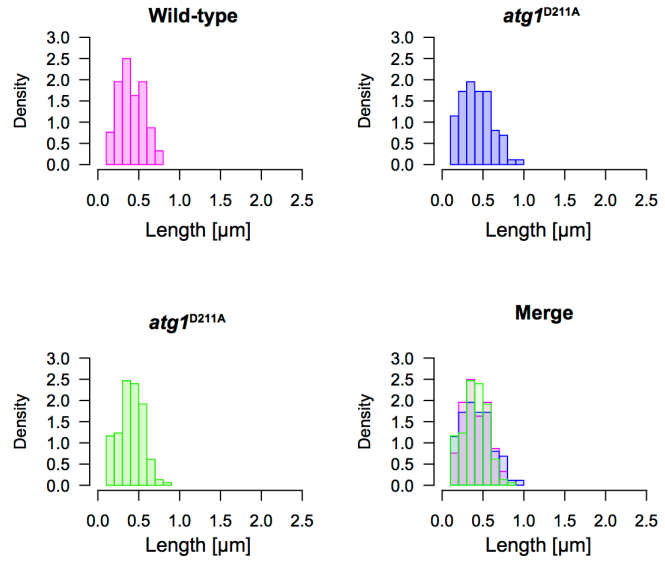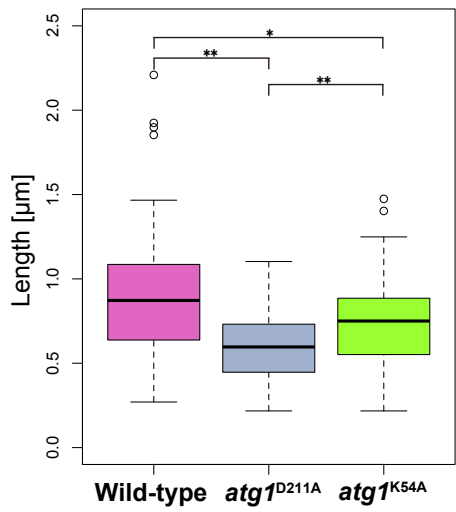
Fig. 9. Size of ARSs after dot-shaped or elongated structure discrimination

After discrimination by randomForest algorism, lengths of the IM and VICS of each strain were compared, respectively. (A) Comparison of structure length of IMs. (B) Histogram of IM length data in each strain. The IM length of wild-type cells is longer than that of *atg1* mutants. The leaky mutant, *atg1*^K54A has longer IM length than *atg1*^D211A. (C) Comparison of structure length of the VICS. (D) Histogram of structure length of VICS in each strain. There was no significant difference between VICS length in these strains. * $P < 0.05$; ** $P < 0.001$; N.S. (not significant) indicates $P > 0.05$ (two tailed Student's *t*-test).

（以降の結果、考察および Part II の内容は学術誌に投稿予定であるため除外した）

Material and methods

Strains and Plasmids

Yeast strains and plasmids are listed in Tables 1 and 2. Cells were cultured in YPD medium (1% yeast extract, 2% bacto-peptone, 2% glucose) or SD/CA medium (0.17% Bacto yeast nitrogen base w/o amino acids and ammonium sulfate, 0.5% ammonium sulfate, 0.5% Bacto casamino acids, 2% glucose) with appropriate supplements. Plasmids were amplified by utilizing Escherichia coli cells in LB medium (1% Bacto tryptone, 0.5% Bacto yeast extract, 1% NaCl). Amplicillin was added to LB medium at a concentration of 60 μg/mL. To induce the Cu2+-inducible CUP1 promoter, cells were cultured for 1 day in SD/CA medium containing 250 μM CuSO4. Rapamycin (0.2 μg/mL) was added to induce autophagy. Each sample was acquired every 30 minutes after addition of rapamycin.

Fluorescence microscopy

Cells were cultured to a concentration of 2.0×10^7 cells/mL in SD/CA medium and cultured with 0.2 μg/mL of rapamycin (1 mg/mL stock dissolved in dimethyl sulfoxide) for 2 hours. Cells were collected with a microcentrifuge, suspended to the remaining medium, and observed by fluorescence microscopy. An IX83 inverted system microscope (Olympus, Japan) and a CoolSNAP HQ CCD camera (Nippon Roper, Japan) were used for image acquisition. U-FGFP and U-FMCHE filter sets (Olympus, Japan) were used for GFP and RFP visualization. Images were acquired with MetaVue software (Molecular Devices)

Confocal fluorescence microscopy

W303 strain background yeast cells were cultured until mid-log phase (2.0×10^7 cells/mL) in filtered YPD medium and cultured with 0.4 μg/mL of rapamycin (1 mg/mL stock dissolved in dimethyl sulfoxide) for 1 hour. Cells were collected with a microcentrifuge, suspended to the remaining medium. Cells were stabilized with 1 mg/ μL Concanavalin A for time-lapse imaging. A FLUOVIEW FV3000 with IX83 inverted system microscope was used for image acquisition. (Olympus, Japan) Images were acquired with FV31S-SW software (Olympus, Japan).

Extraction of ARS from microscopic images

ARSs were extracted from microscopic image with ImageJ software. At first, microscopic images were normalized those fluorescence. ARSs were filtered with a bandpass filter to detect drastic change in intensity. Images were binarized with a threshold value. The threshold value was determined the value that not detect autofluorescence and can detect cup-shaped structure. Binarized structures were analyzed with particle analysis algorism in ImageJ. Nine parameters (area, majour, minor, angle, circularity, axis ratio, roundness and solidity) of each ARSs were extracted by particle analysis.

Discrimination with machine learning

As training data, 336 ARSs were discriminated into VICS or IM manually. Using training data, discriminator was made with randomForest algorism (randomForest version

4.6-10) in R (R version 3.1.3). Extracted 9 parameters from ImageJ were used for this discriminator. In randomForest algorism, discriminator was constructed with group learning of decision tree. Each decision tree makes criteria of VICS or IM based on randomly chose 2 parameters. Half of pre-discriminated data was used for making discriminator and the other half data was used for testing accuracy of discriminator. Importance of each parameter was calculated based on the accuracy rate of decision tree used that parameter. Final accuracy of the discriminator was 91.5%. ARSs were extracted from microscopy image of wild-type SEY6210 (WT), $atg1^{D211A}$ and $atg1^{K54A}$, and discriminated into VICS or IM by machine learning. The half value of perimeter is a parameter that reflects length of cup-shaped structure well. So, a half value of perimeter is called structure length. Structure length of IM and VICS are called IM length and VICS length, respectively. Structural length of VICS and IM were compared in each strain.

Optimization of bandpass filter

To improve the accuracy of Qautas, optimization of filter process were performed. Ground truth data were made by manually with plotting every dot that looks ARS. By using ImageJ macro language, every 45 patterns of filter range between 1 pixel to 10 pixels were generated. Auto-threshold function of ImageJ was used for threshold decision and ARSs were extracted. Difference between extracted area and ground truth data were calculated (Fig. 39). The subtraction of ground truth data from extracted data leaves false positive. The subtraction of extracted data from ground truth data leaves false negative. Precision and Recall were calculated as below formula.

$$\text{Precision} \quad = \frac{\text{True Positive}}{\text{False positive + True positive}}$$

$$\text{Recall} \quad = \frac{\text{True Positive}}{\text{False negative + True positive}}$$

Parameter which showed high-recall score and better precision (filter range 2 to 5px) is used (Fig. 40) .

PCA and hierarchical clustering

To figure out the morphological difference of elongated structure among WT and autophagy mutants, I performed PCA. Nine morphological parameters were subjected to extract the PC. Euclidean distances of each structure were calculated using PC score of PC 1 to 4. Structures were clustered with maximum distance method of hierarchical clustering method. These processes were performed by "R" software.

Clustering with GMM

For the establishment of discriminator for ARSs with non-supervised learning, GMM are constructed by R (version 3. 1. 3). Nine morphological parameter data (area, perimeter, majour length, minor length, angle, circularity, axis ratio roundness and solidity) are subjected to the PCA using "prcomp" command. Library "mclust" (version 5. 0. 1) are used for optimization of distribution number for the model. Before clustering, all data are normalized with distribution and mean value of original data that used for model creation.

Then, normalized data are subjected to the clustering based on GMM.

Three-dimensional image analysis

Fluorescence microscopic images are acquired with confocal microscopy. Time-lapse images are acquired with z stack images are acquired each 41 nm and 1 minute time interval.

Colocalization analysis of fluorescence signals

Fluorescence microscopic images are subjected to normalization of intensity, bandpass filter and binarization.

References

Araki Y, Ku WC, Akioka M, May AI, Hayashi Y, Arisaka F, Ishihama Y, Ohsumi Y. (2013). Atg38 is required for autophagy-specific phosphatidylinositol 3-kinase complex integrity. J Cell Biol. 2013 Oct 28;203(2):299-313.

Baba M, Takeshige K, Baba N, Ohsumi Y. (1994). Ultrastructural analysis of the autophagic process in yeast: detection of autophagosomes and their characterization. J Cell Biol. 1994 Mar;124(6):903-13.

Banerjee R, Beal MF, Thomas B. (2010). Autophagy in neuro- degenerative disorders: Pathogenic roles and therapeutic implications. Trends Neurosci 33: 541–549.

Boutouja F, Stiehm CM, Reidick C, Mastalski T, Brinkmeier R, Magraoui FE, Platta HW. (2019). Vac8 Controls Vacuolar Membrane Dynamics during Different Autophagy Pathways in *Saccharomyces cerevisiae*. Cells. 2019 Jun 30;8(7). pii: E661.

Breiman L. (2001). Random Forests. Machine Learning 45 (1): 5–32.

Cebollero E, van der Vaart A, Zhao M, Rieter E, Klionsky DJ, Helms JB, Reggiori F. (2012). Phosphatidylinositol-3-phosphate clearance plays a key role in autophagosome completion. Curr Biol. 2012 Sep 11;22(17):1545-53.

Chew LH, Lu S, Liu X, Li FK, Yu AY, Klionsky DJ, Dong MQ, Yip CK. (2015). Molecular interactions of the *Saccharomyces cerevisiae* Atg1 complex provide insights into assembly and regulatory mechanisms. Autophagy. 2015;11(6):891-905.

Fujioka Y, Suzuki SW, Yamamoto H, Kondo-Kakuta C, Kimura Y, Hirano H, Akada R, Inagaki F, Ohsumi Y, Noda NN. (2014). Structural basis of starvation-induced assembly of the autophagy initiation complex. Nat Struct Mol Biol. 2014 Jun;21(6):513-21.

Fraley C, Raftery AE, Murphy TB, Scrucca L. (2012). mclust Version 4 for R: Normal Mixture Modeling for Model-Based Clustering, Classification, and Density Estimation.

Graef M, Friedman JR, Graham C, Babu M, Nunnari J. (2013). ER exit sites are physical and functional core autophagosome biogenesis components. Mol Biol Cell. 2013 Sep;24(18):2918-31.

Hirata E, Ohya Y, Suzuki K. (2017). Atg4 plays an important role in efficient expansion of autophagic isolation membranes by cleaving lipidated Atg8 in *Saccharomyces cerevisiae*. PLoS One. 2017 Jul 13;12(7):e0181047.

Huh WK, Falvo JV, Gerke LC, Carroll AS, Howson RW, Weissman JS, O'Shea EK. (2003). Global analysis of protein localization in budding yeast. Nature. 2003 Oct

16;425(6959):686-91.

Jao CC, Ragusa MJ, Stanley RE, Hurley JH. (2013). A HORMA domain in Atg13 mediates PI 3-kinase recruitment in autophagy. Proc Natl Acad Sci USA 110(14):5486–5491.

Kamada Y, Funakoshi T, Shintani T, Nagano K, Ohsumi M, Ohsumi Y. (2000). Tor-mediated induction of autophagy via an Apg1 protein kinase complex. J. Cell Biol., 150, 1507-1513

Kawamata T, Kamada Y, Kabeya Y, Sekito T, Ohsumi Y, (2008). Organization of the Pre-autophagosomal Structure Responsible for Autophagosome Formation. Subramani S, ed. *Molecular Biology of the Cell*. 2008;19(5):2039-2050.

Kawaoka T, Ohnuki S, Ohya Y, Suzuki K. (2017). Morphometric analysis of autophagy-related structures in *Saccharomyces cerevisiae*. Autophagy. 2017;13(12):2104-2110.

Kijanska M, Dohnal I, Reiter W, Kaspar S, Stoffel I, Ammerer G, Kraft C, Peter M. (2010). Activation of Atg1 kinase in autophagy by regulated phosphorylation. Autophagy. 2010 Nov;6(8):1168-78.

Kirisako T, Baba M, Ishihara N, Miyazawa K, Ohsumi M, Yoshimori T, Noda T, Ohsumi

Y. (1999). Formation process of autophagosome is traced with Apg8/Aut7p in yeast. J Cell Biol. 1999 Oct 18;147(2):435-46.

Kotani T, Kirisako H, Koizumi M, Ohsumi Y, Nakatogawa H. (2018) The Atg2-Atg18 complex tethers pre-autophagosomal membranes to the endoplasmic reticulum for autophagosome formation. Proc Natl Acad Sci U S A. 2018 Oct 9;115(41):10363-10368

Kotani T and Nakatogawa H. (2018). Functional analysis of Atg24 during autophagosome formation. Yeast Gebetics and Molecular Biology News japan. September 10-12, 2018 No. 51, p54

Matsuura A, Tsukada M, Wada Y, Ohsumi Y. (1997). Apg1p, a novel protein kinase required for the autophagic process in *Saccharomyces cerevisiae*. Gene. 1997 Jun 19;192(2):245-50.

Mizushima N, Komatsu M. (2011). Autophagy: renovation of cells and tissues. Cell, 147, 728-741

Mizushima N, Yamamoto A, Hatano M, Kobayashi Y, Kabeya Y, Suzuki K, Tokuhisa T, Ohsumi Y, Yoshimori T. (2001). Dissection of autophagosome formation using Apg5-deficient mouse embryonic stem cells. J Cell Biol. 2001 Feb 19;152(4):657-68.

Mizushima N, Yoshimori T, and Ohsumi Y, (2011). The Role of Atg Proteins in Autophagosome Formation, Annual Review of Cell and Developmental Biology Vol. 27: 107-132

Nakatogawa H, Suzuki K, Kamada Y & Ohsumi Y. (2009). Dynamics and diversity in autophagy mechanisms: lessons from yeast. *Nature Reviews Molecular Cell Biology* 10, 458-467

Nice DC, Sato TK, Stromhaug PE, Emr SD, Klionsky DJ. (2002). Cooperative binding of the cytoplasm to vacuole targeting pathway proteins, Cvt13 and Cvt20, to phosphatidylinositol 3-phosphate at the pre-autophagosomal structure is required for selective autophagy. J. Biol. Chem. 277, 30198-30207.

Noda NN and Fujioka Y. (2015). Atg1 family kinases in autophagy initiation. Cell Mol Life Sci. 2015 Aug;72(16):3083-96.

Noda T, Matsuura A, Wada Y, Ohsumi Y. (1995). Novel system for monitoring autophagy in the yeast *Saccharomyces cerevisiae*. Biochem Biophys Res Commun. 1995 May 5;210(1):126-32.

Noda T and Klionsky DJ. (2008). The quantitative Pho8Delta60 assay of nonspecific autophagy. Methods Enzymol. 2008;451:33-42.

Obara K, Sekito T, Niimi K, Ohsumi Y. (2008). The Atg18-Atg2 complex is recruited to autophagic membranes via phosphatidylinositol 3-phosphate and exerts an essential function. J Biol Chem. 2008 Aug 29;283(35):23972-80.

Osawa T, Kotani T, Kawaoka T, Hirata E, Suzuki K, Nakatogawa H, Ohsumi Y, Noda NN. (2019). Atg2 mediates direct lipid transfer between membranes for autophagosome formation. Nat Struct Mol Biol. 2019 Apr;26(4):281-288.

Papinski D, Schuschnig M, Reiter W, Wilhelm L, Barnes CA, Maiolica A, Hansmann I, Pfaffenwimmer T, Kijanska M, Stoffel I, Lee SS, Brezovich A, Lou JH, Turk BE, Aebersold R, Ammerer G, Peter M, Kraft C. (2014). Early Steps in Autophagy Depend on Direct Phosphorylation of Atg9 by the Atg1 Kinase. Mol Cell. 2014 Feb 6;53(3):471-83.

Rao Y, Perna MG, Hofmann B, Beier V, Wollert T. (2016). The Atg1-kinase complex tethers Atg9-vesicles to initiate autophagy. Nat Commun. 2016 Jan 12;7:10338.

Reggiori F, Tucker KA, Stromhaug PE, Klionsky DJ. (2004). The Atg1-Atg13 complex regulates Atg9 and Atg23 retrieval transport from the pre-autophagosomal structure. Dev Cell. 2004 Jan;6(1):79-90.

Ri S. (2019). Comprehensive analysis of autophagosome formation process in *Saccharomyces cerevisiae.* Master thesis. The University of Tokyo.

Rioux JD, Xavier RJ, Taylor KD, Silverberg MS, Goyette P, Huett A, Green T, Kuballa P, Barmada MM, Datta LW, Shugart YY, Griffiths AM, Targan SR, Ippoliti AF, Bernard EJ, Mei L, Nicolae DL, Regueiro M, Schumm LP, Steinhart AH, Rotter JI, Duerr RH, Cho JH, Daly MJ, Brant SR. (2007). Genome-wide association study identifies new susceptibility loci for Crohn disease and implicates autophagy in disease pathogenesis. Nat Genet. 2007 May;39(5):596-604.

Robinson JS, Klionsky DJ, Banta LM, Emr SD. (1988). Protein sorting in *Saccharomyces cerevisiae*: isolation of mutants defective in the delivery and processing of multiple vacuolar hydrolases. Mol Cell Biol. 1988 Nov; 8(11): 4936–4948.

Rubinsztein DC, Codogno P, Levine B. (2012). Nat Rev Drug Discov. Autophagy modulation as a potential therapeutic target for diverse diseases. 2012 Sep;11(9):709-30.

Gómez-Sánchez R, Rose J, Guimarães R, Mari M, Papinski D, Rieter E, Geerts WJ, Hardenberg R, Kraft C, Ungermann C, Reggiori F. (2018). Atg9 establishes Atg2-dependent contact sites between the endoplasmic reticulum and phagophores. J Cell Biol. 2018 Aug 6;217(8):2743-2763.

Sikorski RS and Hieter P. (1989) A system of shuttle vectors and yeast host strains designed for efficient manipulation of DNA in *Saccharomyces cerevisiae*. Genetics. 1989 May;122(1):19-27.

Suzuki K, Akioka M, Kondo-Kakuta C, Yamamoto H, Ohsumi Y. (2013). Fine mapping of autophagy-related proteins during autophagosome formation in *Saccharomyces cerevisiae*. J Cell Sci. 2013 Jun 1;126(Pt 11):2534-44.

Suzuki K, Kirisako T, Kamada Y, Mizushima N, Noda T, Ohsumi Y. (2001). The pre-autophagosomal structure organized by concerted functions of APG genes is essential for autophagosome formation. EMBO J. 2001 Nov 1;20(21):5971-81.

Suzuki K, Kubota Y, Sekito T, Ohsumi Y. (2007). Hierarchy of Atg proteins in pre-autophagosomal structure organization. Genes Cells. 2007 Feb;12(2):209-18.

Suzuki K, Noda T, Ohsumi Y. (2004). Interrelationships among Atg proteins during autophagy in *Saccharomyces cerevisiae*. Yeast. 2004 September 10.1002/yea.1152

Suzuki K and Ohsumi Y. (2007). Molecular machinery of autophagosome formation in yeast, *Saccharomyces cerevisiae*. FEBS Lett. 2007 May 22;581(11):2156-61.

Strømhaug PE, Reggiori F, Guan J, Wang CW, Klionsky DJ. (2004). Atg21 is a

phosphoinositide binding protein required for efficient lipidation and localization of Atg8 during uptake of aminopeptidase I by selective autophagy. Mol Biol Cell. 2004 Aug;15(8):3553-66.

Tsukada M. and Ohsumi Y. (1993). Atg FEBS Volume 333, Issues 1–2, 25 October 1993, Pages 169–174

White E. (2012). Deconvoluting the context-dependent role for autophagy in cancer. Nat Rev Cancer. 2012; Apr 26;12(6):401-10.

Yamamoto H, Kakuta S, Watanabe TM, Kitamura A, Sekito T, Kondo-Kakuta C, Ichikawa R, Kinjo M, Ohsumi Y. (2012). Atg9 vesicles are an important membrane source during early steps of autophagosome formation. J Cell Biol. 2012 Jul 23;198(2):219-33.

Yeh Y, Wrasman K, Herman PK. (2010). Autophosphorylation Within the Atg1 Activation Loop Is Required for Both Kinase Activity and the Induction of Autophagy in *Saccharomyces cerevisiae.* Genetics,July 2010 vol. 185 no. 3 871-882

Zhou F, Wu Z, Zhao M, Murtazina R, Cai J, Zhang A, Li R, Sun D, Li W, Zhao L, Li Q, Zhu J, Cong X, Zhou Y, Xie Z, Gyurkovska V, Li L, Huang X, Xue Y, Chen L, Xu H, Xu H, Liang Y, Segev N. (2019). Rab5-dependent autophagosome closure by ESCRT. J Cell Biol. 2019 Jun 3;218(6):1908-1927.

Zhou F, Zou S, Chen Y, Lipatova Z, Sun D, Zhu X, Li R, Wu Z, You W, Cong X, Zhou Y, Xie Z, Gyurkovska V, Liu Y, Li Q, Li W, Cheng J, Liang Y, Segev N. (2017). A Rab5 GTPase module is important for autophagosome closure. PLoS Genet. 2017 Sep 21;13(9):e1007020.

Tables

Table 1. Yeast strains used in this study

Strain	Genotype	Source
SEY6210	*MATα lys2 suc2 his3 leu2 trp1 ura3*	Robinson *et al*., 1988
YMM275	SEY6210 *MATα lys2 suc2 his3 leu2 trp1 ura3 ATG1-2×GFP:kanMX*	Suzuki *et al*., 2013
ScHY-019	SEY6210 *MATα lys2 suc2 his3 leu2 trp1 ura3 atg1Δ::atg1(D211A):kanMX*	Suzuki *et al*., 2013
ScHY-003	SEY6210 *MATα lys2 suc2 his3 leu2 trp1 ura3 atg1Δ::atg1(K54A):kanMX*	Suzuki *et al*., 2013
GYS103	SEY6210 *MATα lys2 suc2 his3 leu2 trp1 ura3 atg1Δ::URA3*	Suzuki *et al*., 2004
YOC5332	SEY6210 *MATα lys2 suc2 his3 leu2 trp1 ura3 atg1Δ::cgURA3*	This study
GYS639	SEY6210 *MATα lys2 suc2 his3 leu2 trp1 ura3 atg1Δ::kanMX*	Suzuki *et al*., 2013
GYS645	SEY6210 *MATα lys2 suc2 his3 leu2 trp1 ura3 atg2Δ::kanMX*	Suzuki *et al*., 2013
YNH1000	SEY6210 *MAT**a** Leu2::GFPATG8-h*	From Dr, Nakatogawa
TYS075	SEY6210 *MAT**a** Leu2::GFPATG8-h atg1Δ:kanMX*	This study
GYS1117	SEY6210 *MATα pho8d60, Sec13-2XGFPhy::kanMX6, pRS316[2xmCherry-ATG8]*	From Dr. Suzuki
GYS1118	SEY6210 *MATα pho8d60, Sec13-2XGFPhy::kanMX6, atg1d::LEU2, pRS316[2xmCherry-ATG8]*	From Dr. Suzuki
GYS1119	SEY6210 *MATα pho8d60, Sec13-2XGFPhy::kanMX6, atg2d::LEU2, pRS316[2xmCherry-ATG8]*	From Dr. Suzuki
TYS40	SEY6210 *MATα lys2 suc2 his3 leu2 trp1 ura3 ATG1- 2×mNeonGreen:KanMX*	This study
TYS93	SEY6210 *MATα lys2 suc2 his3 leu2 trp1 ura3 ATG11- 2×mNeonGreen:KanMX*	This study
TYS87	SEY6210 *MATα lys2 suc2 his3 leu2 trp1 ura3 ATG13- 2×mNeonGreen:KanMX*	This study
TYS94	SEY6210 *MATα lys2 suc2 his3 leu2 trp1 ura3 ATG17- 2×mNeonGreen:KanMX*	This study
TYS88	SEY6210 *MATα lys2 suc2 his3 leu2 trp1 ura3 ATG29- 2×mNeonGreen:KanMX*	This study
TYS89	SEY6210 *MATα lys2 suc2 his3 leu2 trp1 ura3 ATG31- 2×mNeonGreen:KanMX*	This study
GYS1015	W303 *MAT**a** ADE2 leu2-3 his3-11, 15 trp1-1 ura3-1 can1-100*	From Dr. Suzuki
YOC5525	W303 *MATα ADE2 leu2-3 his3-11, 15 trp1-1 ura3-1 can1-100*	From Mr. Ri
TYS187	*MAT**a**/α lys2 suc2 his3 leu2 trp1 ura3 atg1Δ::ATG1-mNeonGreen:kanMX atg8Δ::2×mRuby-Atg8:HIS3*	This study
TYS188	*MAT**a**/α lys2 suc2 his3 leu2 trp1 ura3 atg2Δ::ATG2-mNeonGreen:kanMX atg8Δ::2×mRuby-Atg8:HIS3*	This study
TYS189	*MAT**a**/α lys2 suc2 his3 leu2 trp1 ura3 atg5Δ::ATG5-mNeonGreen:kanMX atg8Δ::2×mRuby-Atg8:HIS3*	This study
TYS195	*MAT**a**/α lys2 suc2 his3 leu2 trp1 ura3 atg9Δ::ATG9-mNeonGreen:kanMX atg8Δ::2×mRuby-Atg8:HIS3*	This study
TYS191	*MAT**a**/α lys2 suc2 his3 leu2 trp1 ura3 atg11Δ::ATG11-mNeonGreen:kanMX atg8Δ::2×mRuby-Atg8:HIS3*	This study
TYS192	*MAT**a**/α lys2 suc2 his3 leu2 trp1 ura3 atg17Δ::ATG17-mNeonGreen:kanMX atg8Δ::2×mRuby-Atg8:HIS3*	This study

TYS193	*MAT**a**/α lys2 suc2 his3 leu2 trp1 ura3 atg27Δ::ATG27-mNeonGreen:kanMX atg8Δ::2×mRuby-Atg8:HIS3*	This study
TYS206	*MAT**a**/α lys2 suc2 his3 leu2 trp1 ura3 atg20Δ::ATG20-mNeonGreen:kanMX atg8Δ::2×mRuby-Atg8:HIS3*	This study
TYS207	*MAT**a**/α lys2 suc2 his3 leu2 trp1 ura3 atg24Δ::ATG24-mNeonGreen:kanMX atg8Δ::2×mRuby-Atg8:HIS3*	This study

Table 2. Plasmids used in this study

Name	Properties	Marker	Source
pRS314	Centromeric plasmid	*TRP1*	Sikorski & Hieter 1989
pRS316	Centromeric plasmid	*URA3*	Sikorski & Hieter 1989
pYEX-BX[prApe1]	Plasmid for expression of prApe1 from the *CUP1* promoter	*URA3*	Suzuki *et al.*, 2013
pRS314[mNeonGreen-*ATG8*]	Plasmid for expression of mNeonGreen-Atg8	*TRP1*	From Dr. Yoshinori Ohsumi
pRS305[BFP-APE1]	Plasmid for integration of *BFP-APE1*	*LEU2*	From Dr. Daniel J. Klionsky
pRS316[*ATG1*]	Plasmid for expression of wild-type *ATG1*	*URA3*	From Dr. Suzuki
pRS305[mRFP-*APE1*]	Plasmid for integration of *mRFP-APE1*	*LEU2*	Stromhaug *et al.*, 2004
pRS426[Ape1-EBFP]	Plasmid for expression of APE1-EBFP from the *CUP1* promoter	*URA3*	From Dr. Noda
pFA6a[2xmNeonGreen]	Plasmid for integration 2xNeonGreen	*kanMX*	From Dr. Yoshinori Ohsumi
pYO2244	Plasmid for replacement with *URA3*	*URA3*	Lab. Stock
pRS314[GFP-*ATG8*]	Plasmid for expression of GFP-Atg8	*TRP1*	Suzuki *et al.*, 2001
pRS303[2xmRuby-*ATG8*]	Plasmid for expression of 2xmRuby-Atg8	*HIS3*	Lab. Stock

Table 3. Loadings of parameters for PCs

	PC1	PC2	PC3	PC4	PC5	PC6	PC7	PC8	PC9
Area	-0.811	-0.561	0.047	-0.114	0.046	-0.036	0.004	-0.086	0.048
Perim.	-0.932	-0.335	0.000	0.046	0.001	0.006	0.110	-0.005	-0.068
Major	-0.931	-0.192	0.097	-0.272	0.055	0.006	0.026	0.085	0.046
Minor	-0.495	-0.858	0.007	-0.003	-0.045	0.016	-0.126	0.017	-0.036
Angle	0.073	-0.005	0.973	0.220	-0.011	0.000	0.001	0.000	0.000
Circ.	0.853	-0.328	0.105	-0.320	0.225	-0.006	-0.004	-0.002	-0.027
AR	-0.644	0.682	0.096	-0.287	0.029	0.161	-0.034	-0.027	-0.012
Round	0.590	-0.719	-0.101	0.314	0.003	0.154	0.042	0.004	0.027
Solidity	0.664	-0.341	0.142	-0.629	-0.161	0.011	0.035	-0.007	-0.001